Science Advances

AAAS

Supplementary Materials for

Ultra-large electric field–induced strain in potassium sodium niobate crystals

Chengpeng Hu, Xiangda Meng, Mao-Hua Zhang, Hao Tian*, John E. Daniels, Peng Tan, Fei Huang, Li Li, Ke Wang*, Jing-Feng Li, Qieni Lu, Wenwu Cao, Zhongxiang Zhou*

*Corresponding author. Email: tianhao@hit.edu.cn (H.T.); wang-ke@tsinghua.edu.cn (K.W.); zhouzx@hit.edu.cn (Z.Z.)

This PDF file includes:

Supplementary Text

Strain versus electric field curves of the KNN single crystals

We have measured the strains of crystals with different compositions and found that their strains vary greatly. We find that the composition range of the samples with large strain is very narrow. As a result, it is difficult to obtain crystals with exactly the same composition after the sample is subjected to cutting and grinding operations. And the strains of KNN crystals with a slightly compositional deviation from KNN43 crystal are shown in Fig. S1. Although the loops in Fig. S1 are not exactly the same as those in Fig. 1, the deviation is normal for piezoelectric materials. The results confirm that the KNN43 crystals have ultrahigh piezoelectric properties and stable repeatability. In addition, once the composition changed more, the strain and $d_{33}*$ decreased down to 0.06% and 200 pm V^{-1}, respectively, as shown in Fig. S10b.

Spatial strain distribution by the Mach-Zehnder system

The strain vs. electric field shown in Fig. S3 was determined via Mach-Zehnder system (Fig. S2), which is able to confirm the displacement on the whole surface. The sample was polished and sputtered with gold electrode on $(001)_C$ surface, from which the laser was reflected. Then the sample is fixed to the slide with AB glue in the Mach-Zehnder system, and a pulsed electric field (1 kV mm^{-1}) of 1 Hz is applied. Finally, 15 pictures of interference pattern were taken via CCD. With the difference between the interference patterns, the electric field dependence of displacement can be calculated.

When the object light wave and the reference light wave form interference fringes on the CCD, the interference field distribution information will be recorded. In this case, a digital calculation method is required to complete the physical process representing optical reproduction. Here we use the angular spectrum reconstruction algorithm to achieve hologram reproduction. Assuming that the object light wave distribution on the hologram surface is $O(x, y; 0)$, the angular spectrum information $\tilde{O}(k_x, k_y; z)$ on the z plane can be calculated

$$\tilde{O}(k_x, k_y; z) = \mathrm{FT}\{O(x, y; 0)\}\exp ik_z z \tag{1}$$

Where k_x and k_x are the spatial frequency in the x and y directions, respectively. And

$$k_z = \sqrt{\mathrm{k}^2 - k_x^2 - k_y^2}$$

Then the real image reproduces the light field distribution on the image surface as

$$O'(x', y'; 0) = FT^{-1}\left\{\tilde{O}(k_x, k_y; z)\right\} \tag{2}$$

Its phase distribution can be expressed as

$$\delta(x', y') = \arctan \frac{\operatorname{Im} O'(x', y'; 0)}{\operatorname{Re} O'(x', y'; 0)} \tag{3}$$

Where Re and Im in the equation are the real and imaginary parts of the complex amplitude, respectively.

If the digital holograms records the interference distribution fields under two different applied electric field, and the reconstructed complex amplitude of object wave from the hologram surface of them are expressed as $O_1'(x', y')$ and $O_2'(x', y')$, respectively, the corresponding phase distributions $\delta_1(x', y')$ and $\delta_2(x', y')$ can be obtained

$$\delta_i(x', y') = \arctan \frac{\operatorname{Im} O_i'(x', y'; 0)}{\operatorname{Re} O_i'(x', y'; 0)}, \quad i = 1, 2 \tag{4}$$

The phase difference of object can be written as

$$\Delta\delta(x', y') = \begin{cases} \delta_1(x', y') - \delta_2(x', y') & \delta_1(x', y') \geq \delta_2(x', y') \\ \delta_1(x', y') - \delta_2(x', y') + 2\pi & \delta_1(x', y') \leq \delta_2(x', y') \end{cases} \tag{5}$$

Where $\Delta\delta(x', y')$ reflects the relative phase change of each point of the object field. The larger the amount of phase change, the more interference fringes of the interference light field. The corresponding displacement change can be obtained from the correspondence between phase and displacement.

$$\Delta L = \frac{\lambda \Delta \delta(x', y')}{4\sqrt{2}\pi} \qquad (6)$$

Where λ is wavelength, ΔL is the displacement change.

In general, in order to avoid phase unwrapping, it is necessary to reduce the recording time interval to obtain more information of interference distribution fields.

Dielectric properties of the KNN43 single crystals

As shown in fig. S5, the temperature dependence of permittivity and dielectric loss (cooling from 540 to 30 °C) was measured at the frequency of 1 kHz. There are two dielectric anomalies at 175 °C and 418 °C, respectively, indicating the presence of three distinct phases over the temperature range. The phase structures are the orthorhombic structures from room temperature to 175 °C, a tetragonal structure between 175 °C and 418 °C, and a cubic structure above 418 °C. The dielectric constant and dielectric loss are 350 and 0.03 at room temperature, respectively. The additional electrical parameters are shown in Table S2.

Hysteresis loops of the KNN43 crystals

As shown in fig. S9, the ferroelectric hysteresis loops were performed at room temperature with a frequency of 100 Hz. The positive and negative coercive fields are 0.9 kV mm^{-1} and 0.65 kV mm^{-1}, respectively, which means there is an internal electric field in the crystal. The remnant polarization is approximately 13.7 µC cm^{-2} at an electric field of 3.5 kV mm^{-1}. The ferroelectric loops are not sufficiently square

shaped, showing a slight leakage, which is also normal phenomenon observed for lead-based ferroelectric single crystals with complex composition.

Domain structure analyzed by PFM and PLM

Domain structure of samples with different compositions ($x = 0.3 – 0.46$) are observed, as shown in Fig. S11and Fig. S12. Large stripe domains are obtained for samples with x value smaller than 0.40. And the large domains are absent and replaced by smaller herringbone domains between $x = 0.41 – 0.43$. At $x = 0.44 – 0.46$, the herringbone domains disappear, while the labyrinthine domains appear. The PFM images confirm the existence of nanoscale domain structures in $K_{0.43}Na_{0.57}NbO_3$ and $K_{0.45}Na_{0.55}NbO_3$ single crystals, indicating that the domain structure in the $K_{0.43}Na_{0.57}NbO_3$ crystal is more complex than that in $K_{0.45}Na_{0.55}NbO_3$ and $K_{0.37}Na_{0.63}NbO_3$ crystals.
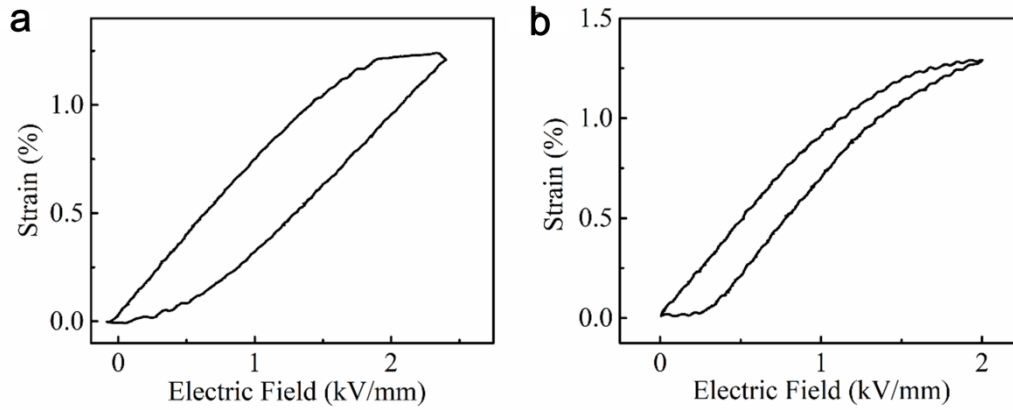
Fig. S1. Strain versus electric field curves. a, Strain versus electric field curves for K$_{0.43}$Na$_{0.57}$NbO$_3$ crystals (abbreviated as KNN43-2) measured by using a ferroelectric test system (Precision Premier II, Radiant Technology, Inc., Albuquerque, NM, USA) at 25 °C. The maximum strain is 1.25% at an electric field of 2.5 kV mm^{-1} at a frequency of 1 Hz. **b**, Strain versus electric field curves for other K$_{0.43}$Na$_{0.57}$NbO$_3$ crystals (abbreviated as KNN43-3) measured by Precision Premier II ferroelectric test system at 25 °C. The maximum strain is 1.25% at an electric field of 2 kV mm^{-1} and a frequency of 1 Hz.
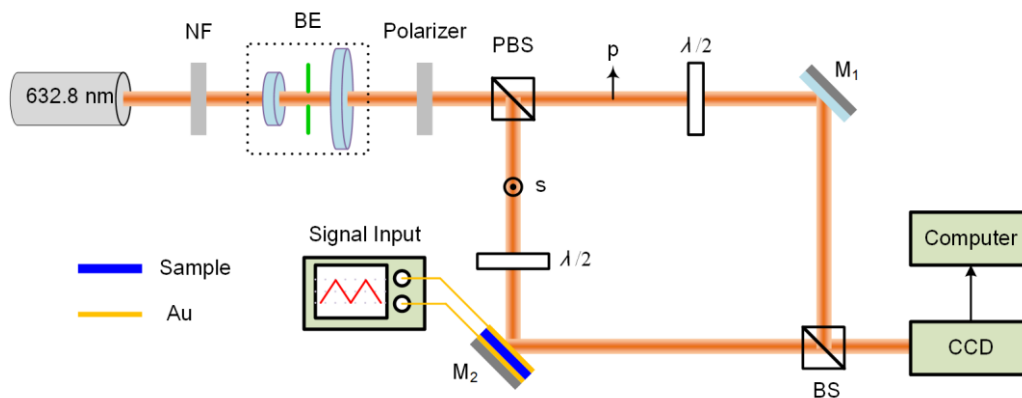

Fig. S2. Mach-Zehnder system. Mach-Zehnder digital holographic interferometry. NF: variable neutral density filter; BE: beam expander, spatial filter, and collimator; PBS: polarizing beam splitter; BS: beam splitter; M1–M2: mirror; and lambda/2: half-wave plate.
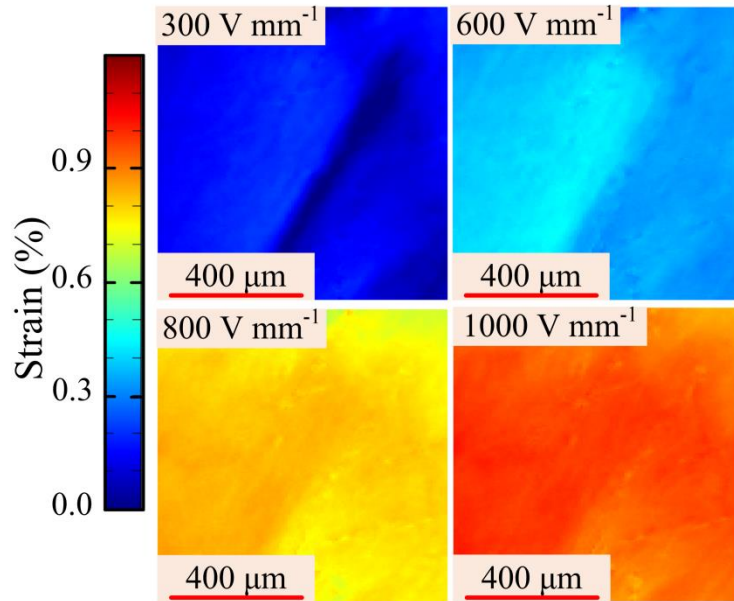
Fig. S3. Images of the spatial strain distribution. The strain versus electric field for the KNN43 crystal was measured using a Mach-Zehnder system at 25 °C. The Mach-Zehnder digital holographic interferometry was introduced to detect the strain response of a given surface, also indicating a large strain of 1% at 1.0 kV mm^{-1}. The strain response was relatively uniform for the entire surface and exhibited a consistent behaviour with the strain curve by gradually increasing the electric field.
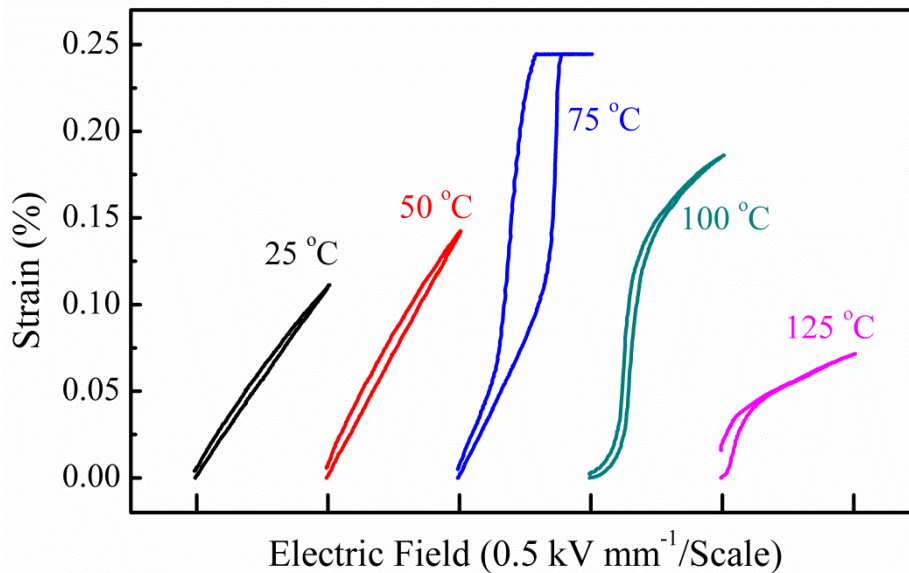

Fig. S4. Strain versus electric field curves. Strain versus electric field curves at varying temperatures between 25 °C and 125 °C for the PMN-33PT crystal at an electric field of 0.5 kV mm^{-1}. The measurements were conducted using an optical probe system at a frequency of 1 Hz. Clearly, there is an electric field-induced phase transition at 75 °C, implying metastable phases over a finite range of fields. The gradient of the *S-E* loop is 2200 pm V^{-1} at 25 °C.
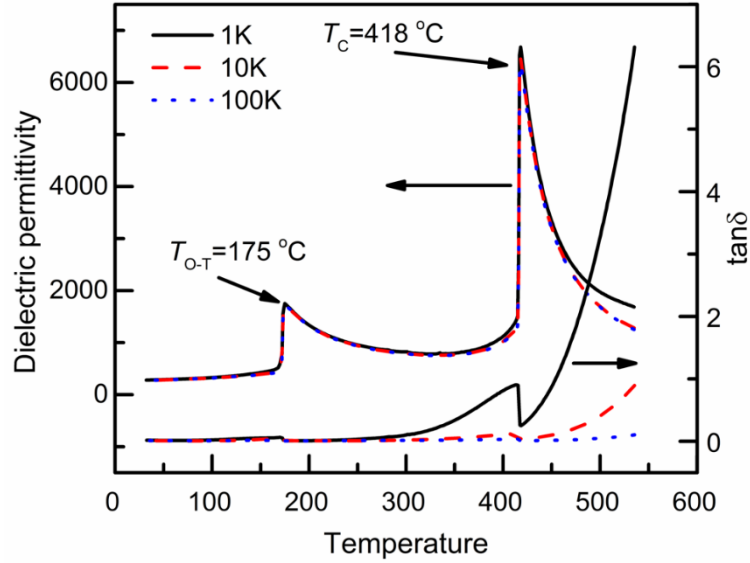
Fig. S5. Dielectric properties. Temperature dependence of the dielectric permittivity of the KNN single crystals at 1 kHz, 10 kHz and 100 kHz. The phase structures are the orthorhombic structures from room temperature to 175 °C, a tetragonal structure between 175 °C and 418 °C, and a paraelectric cubic structure above 418 °C.
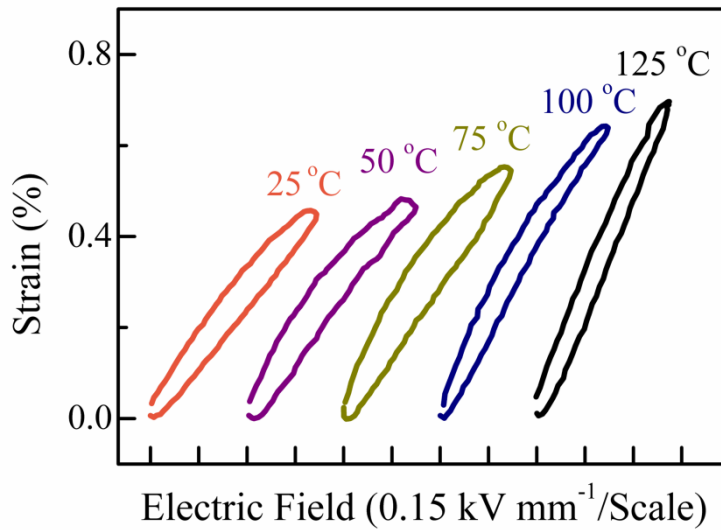

Fig. S6. Temperature dependence of unipolar strain. Strain versus electric field curves at different temperatures for the KNN43 crystal at a low electric field of approximately 0.5 kV mm^{-1}. The measurements were made using an optical probe system at a frequency of 1 Hz. The temperature-insensitive strain behaviours were observed from 25 °C to 125 °C. The gradient of the S-E loop is approximately 9000 pm V^{-1} at 25 °C. With increasing temperature, the value of $d_{33}*$ increases slightly from 9000 to 9900 pm V^{-1} before 75 °C and exhibits a reduction of approximately 30% at 100 °C.
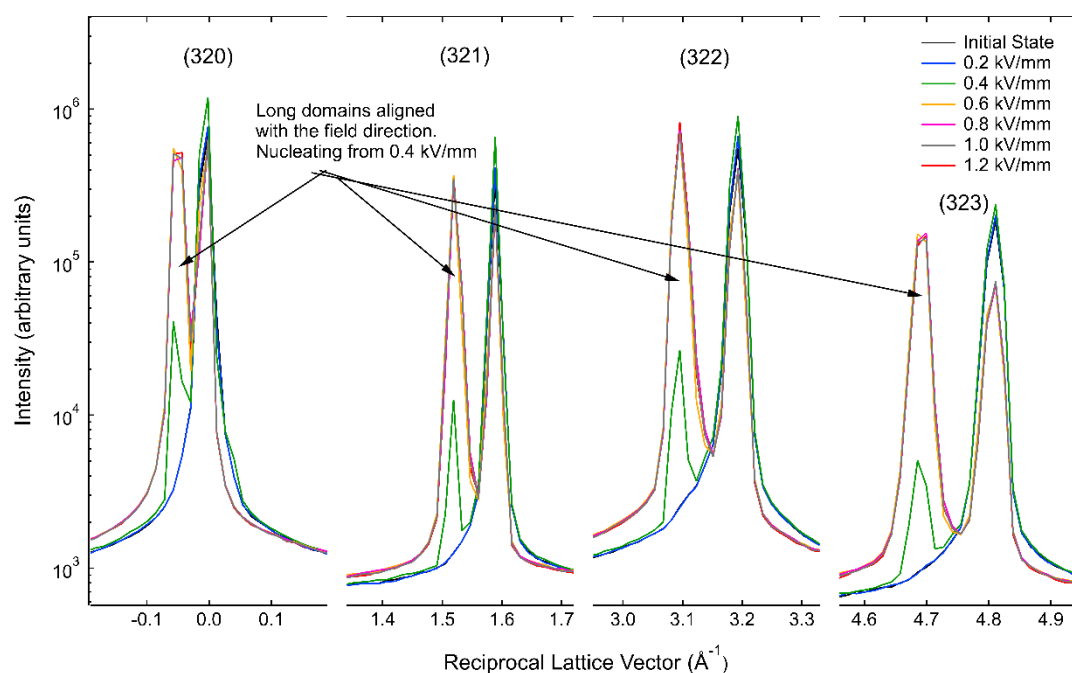
Fig. S7. Development of the long-axis domains parallel to the field direction. Line scan along 31*l* reciprocal space direction. The evolution of low-q peaks is observed at each reflection, indicating the development of long-axis domains parallel to the field direction. The evolution occurs between 0.2 kV mm^{-1} and 0.6 kV mm^{-1}.
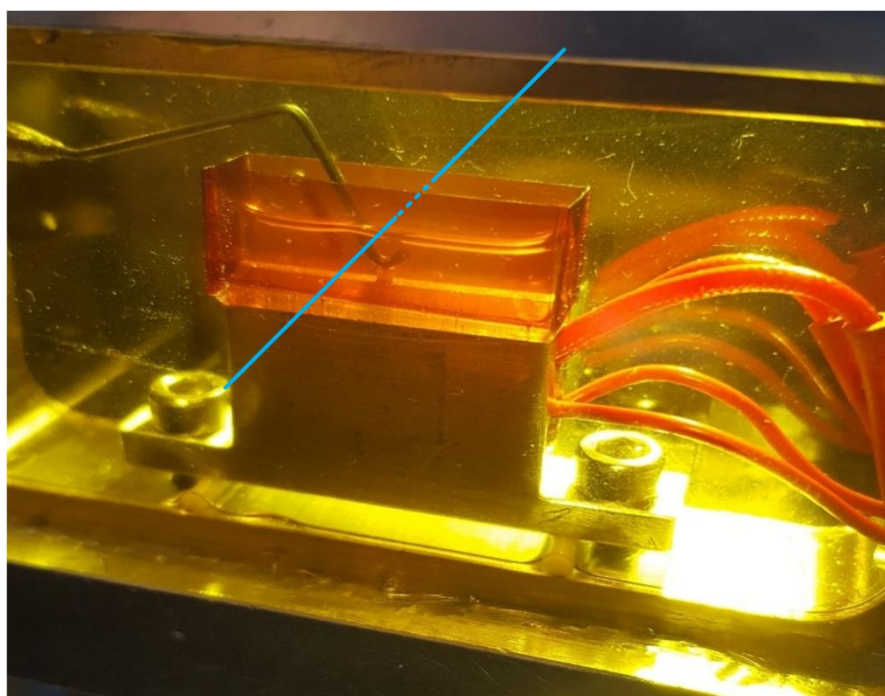

Fig. S8. Single crystal of KNN mounted in an electric field cell. Beam transmission, as shown by the blue line. The sample was rotated around the vertical direction. The field was applied between the top electrode and bottom grounding. During the measurement, the temperature sensor in the cell was read at 24 °C. Photo credit: J. Daniels, UNSW Sydney.
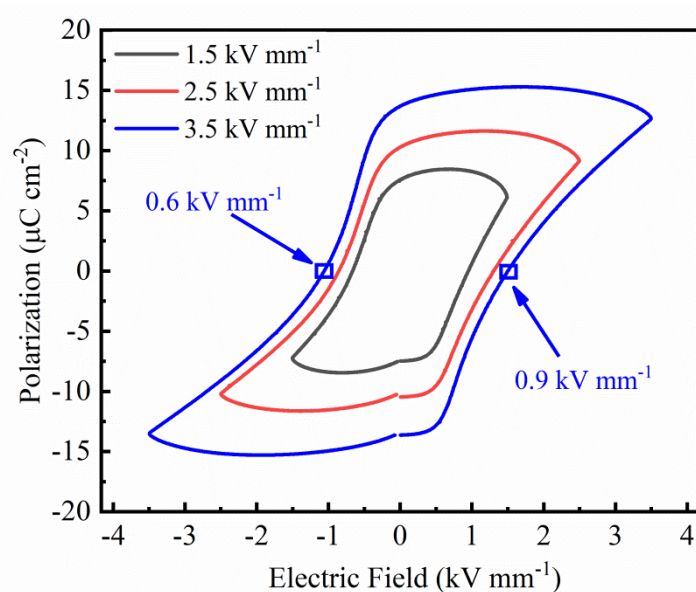
Fig. S9. Hysteresis loops of the KNN43 crystals. The measurements were performed at room temperature and at a frequency of 100 Hz. The value of the remnant polarization is approximately 13.7 μC cm^{-2} at an electric field of 3.5 kV mm^{-1}.

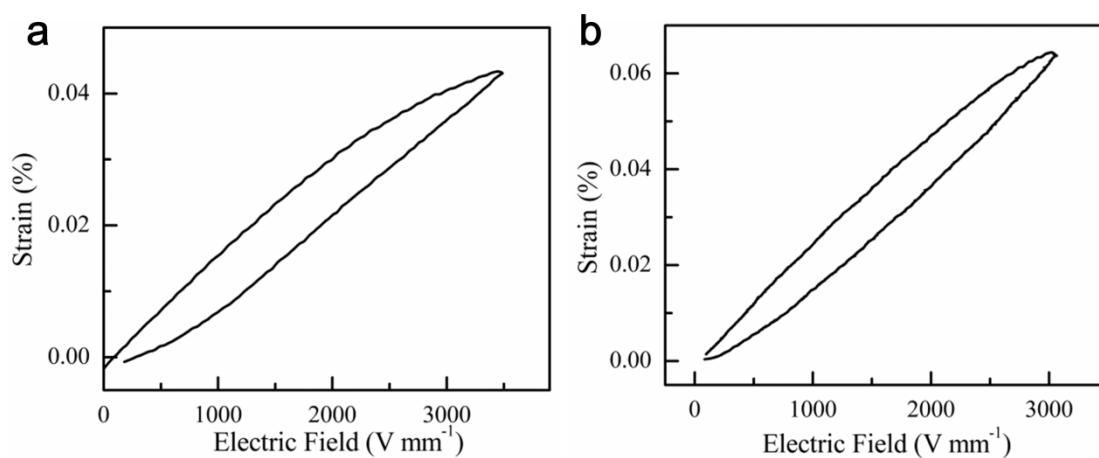**Fig. S10. Strain versus electric field curves.** Plots of the strain versus electric field for **a**, $K_{0.35}Na_{0.65}NbO_3$ and **b**, $K_{0.44}Na_{0.56}NbO_3$ crystals were measured for comparison. The maximum strain is approximately 0.04% at an electric field of 3.5 kV mm^{-1} and 0.06% at an electric field of 3 kV mm^{-1} for $K_{0.35}Na_{0.65}NbO_3$ and $K_{0.44}Na_{0.56}NbO_3$ crystals, respectively. The gradient of the S-E loop is approximately 114 pm V^{-1} and 200 pm V^{-1}; these values are much smaller than the value for the KNN43 crystal.
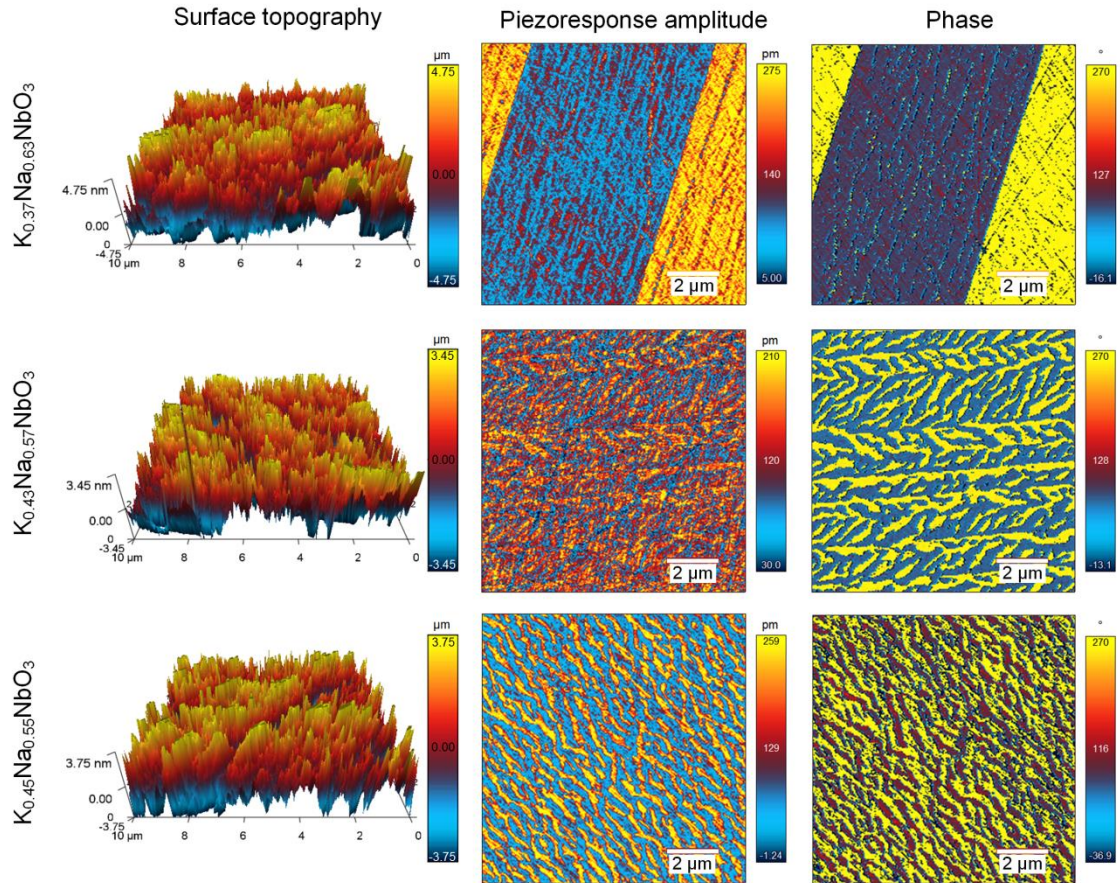
Fig. S11. Vertical PFM images of the domains. Surface morphology, piezoelectric amplitude and PFM phase images of the $K_{0.37}Na_{0.63}NbO_3$, $K_{0.43}Na_{0.57}NbO_3$ and $K_{0.45}Na_{0.55}NbO_3$ single crystals. The sample with a smooth surface was prepared at a scale of 10×10 μm^2. Slight traces of the morphology of the measured area are observed in all samples. The PFM images confirm the existence of nanoscale domain structures in $K_{0.43}Na_{0.57}NbO_3$ and $K_{0.45}Na_{0.55}NbO_3$ single crystals, further indicating that the domain structure in the $K_{0.43}Na_{0.57}NbO_3$ crystal is more complex than that in the $K_{0.45}Na_{0.55}NbO_3$ crystal. This complexity could be the source of the ultra-large electric field-induced strain in the potassium sodium niobate crystals in this work.
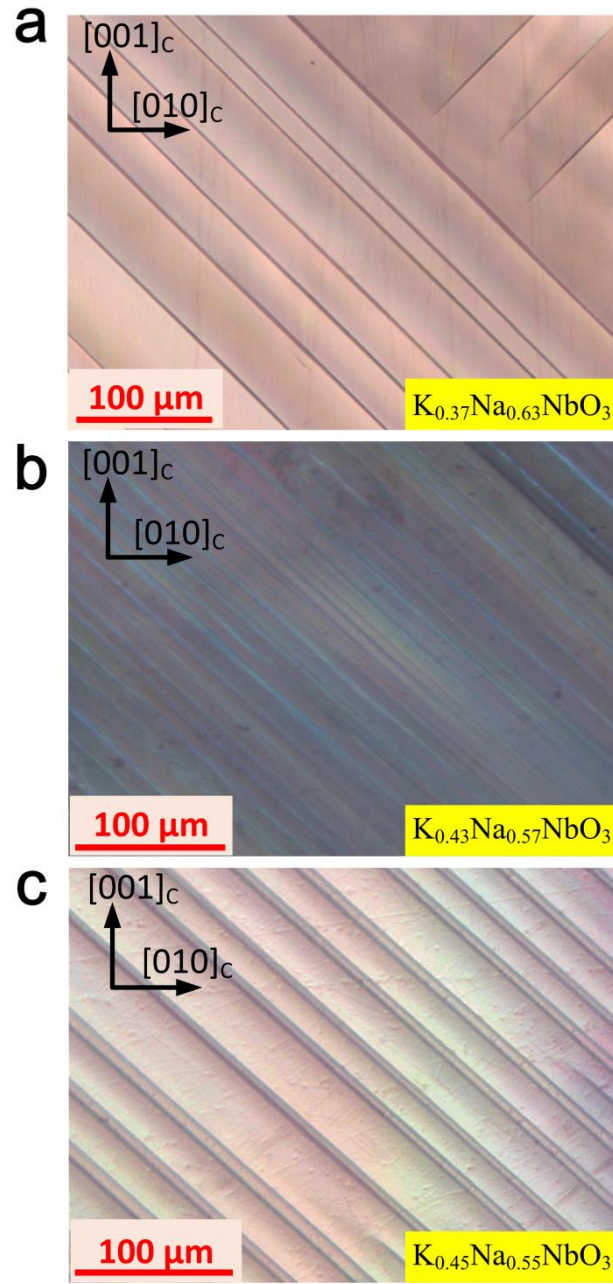
Fig. S12. The domain configuration of the KNN single crystals by using PLM. a, $K_{0.37}Na_{0.63}NbO_3$; **b,** $K_{0.43}Na_{0.57}NbO_3$; and **c,** $K_{0.45}Na_{0.55}NbO_3$ single crystals.
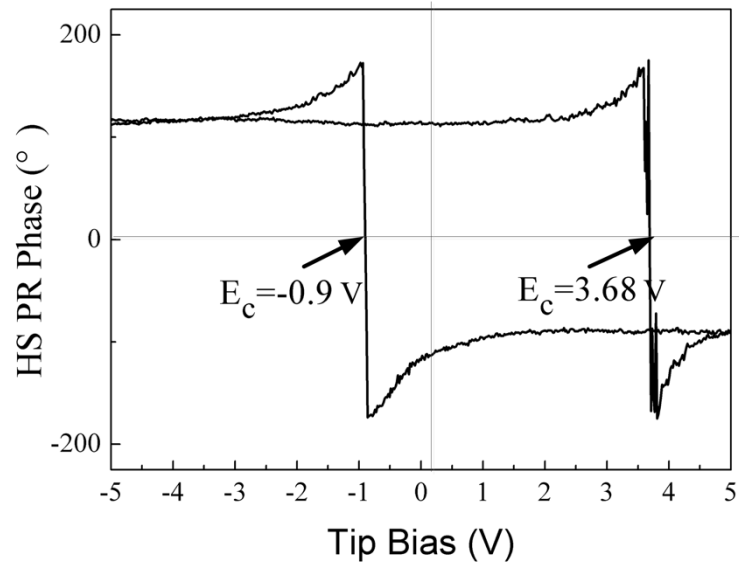
Fig. S13. Phase-voltage hysteresis loop of the $K_{0.37}Na_{0.63}NbO_3$ single crystal by PFM. The PFM phase is reversed when the voltage is reversed, showing a possible polarization reversal of the ferroelectricity. However, this reversal phenomenon has a very obvious bias, as the positive voltage and negative voltage are 3.68 V and -0.9 V, respectively, indicating that one of the polarization reversals requires a higher DC voltage. The existence of a strong spontaneous polarization inside the crystal may be the possible reason for this phenomenon.
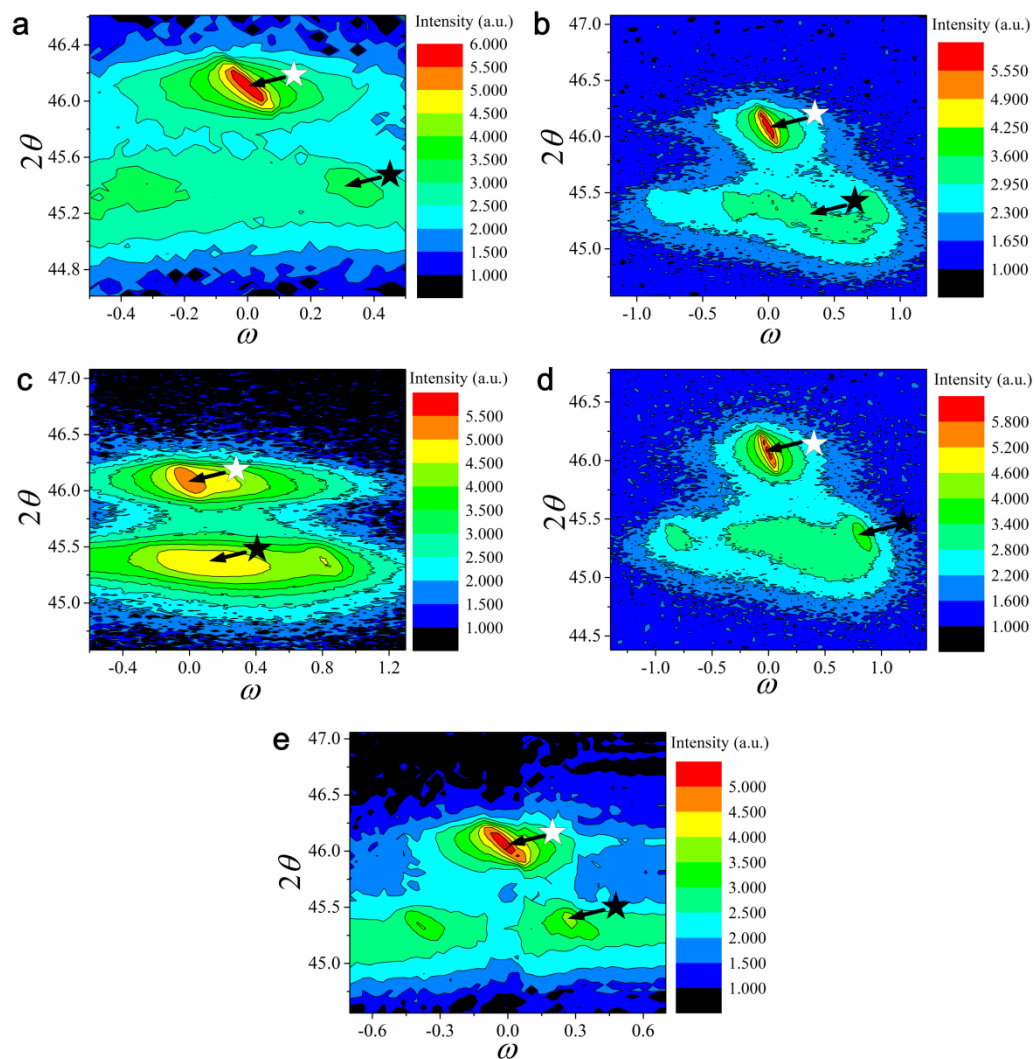
Fig. S14. Reciprocal space maps for the KNN single crystals. The structures of these crystals were studied using XRD reciprocal space mapping. The open and closed stars correspond to the diffraction peaks of (200) and (002) reflections, respectively, used for the calculation in **a**, $K_{0.41}Na_{0.59}NbO_3$; **b**, $K_{0.42}Na_{0.58}NbO_3$; **c**, $K_{0.43}Na_{0.57}NbO_3$; **d**, $K_{0.44}Na_{0.56}NbO_3$; and **e**, $K_{0.45}Na_{0.55}NbO_3$ crystals. It can be calculated that the value of the c/a-lattice parameter of the KNN crystals gradually decreases as the element of potassium increases.

Table S1. Lattice parameter ratio *c/a* of the KNN crystals.

Crystals	c/a
$K_{0.41}Na_{0.59}NbO_3$	1.01566
$K_{0.42}Na_{0.58}NbO_3$	1.01545
$K_{0.43}Na_{0.57}NbO_3$	1.01524
$K_{0.44}Na_{0.56}NbO_3$	1.01501
$K_{0.45}Na_{0.55}NbO_3$	1.01460

Table S2. Properties of the KNN43 crystal.

Properties	KNN43 crystal
Strain (%, 1 kV mm^{-1})	0.9
S/E (pm V^{-1}, 1 kV mm^{-1})	9000
d_{33} meter (pC N^{-1})	170
$\varepsilon_r(\varepsilon_0)$ (100 kHz, poled)	350
tan δ	0.03
E_C (kV mm^{-1})	0.78
P_r (μC cm^{-2})	13.7
$T_{O\text{-}T}$ (°C; cooling)	175
T_C (°C)	418

EMPA information of $K_{0.41}Na_{0.59}NbO_3$ single crystal

Table S3. Measured elemental composition of $K_{0.41}Na_{0.59}NbO_3$ single crystal.

Element	Mass(%)	Atom(%)
Na	7.361	10.7040
Nb	54.589	19.6411
K	8.808	7.5308
O	29.734	62.1242
Total	100.492	100

EMPA information of $K_{0.43}Na_{0.57}NbO_3$ single crystal

Table S4. Measured elemental composition of $K_{0.43}Na_{0.57}NbO_3$ single crystal.

Element	Mass(%)	Atom(%)
Na	7.203	10.5419
Nb	54.631	19.7853
K	9.056	7.7931
O	29.424	61.8796
Total	100.314	100

EMPA information of $K_{0.44}Na_{0.56}NbO_3$ single crystal

Table S5. Measured elemental composition of $K_{0.44}Na_{0.56}NbO_3$ single crystal.

Element	Mass(%)	Atom(%)
Na	6.966	10.2454
Nb	54.166	19.714
K	9.377	8.1096
O	29.303	61.9311
Total	99.812	100